Ferroic nanoclusters in relaxors: the effect of oxygen vacancies

2007 J. Phys.: Condens. Matter 19 246220

(http://iopscience.iop.org/0953-8984/19/24/246220)

IOP PUBLISHING JOURNAL OF PHYSICS: CONDENSED MATTER

J. Phys.: Condens. Matter **19** (2007) 246220 (10pp) doi:10.1088/0953-8984/19/24/246220

Ferroic nanoclusters in relaxors: the effect of oxygen vacancies

B Mihailova[1,5], M Gospodinov[2], B Güttler[3], D Petrova[4], R Stosch[3] and U Bismayer[1]

[1] Mineralogisch-Petrographisches Institut, Universität Hamburg, Grindelallee 48, D-20146 Hamburg, Germany
[2] Institute of Solid State Physics, Bulgarian Academy of Sciences, Boulevard Tzarigradsko Chausee 72, 1784 Sofia, Bulgaria
[3] Physikalisch-Technische Bundesanstalt, Bundesallee 100, 38116 Braunschweig, Germany
[4] South-West University 'Neofith Rilski' Ivan Mihailov Street 66, 2700 Blagoevgrad, Bulgaria

E-mail: mi0a007@uni-hamburg.de

Received 17 October 2006, in final form 6 May 2007
Published 25 May 2007
Online at stacks.iop.org/JPhysCM/19/246220

Abstract

Single crystals of $PbSc_{0.5}Ta_{0.5}O_3$ with suppressed and enhanced oxygen deficiencies and different degrees of long-range B-site ordering were studied by Raman spectroscopy in order to clarify the significance of the different factors for the formation and growth of ferroic clusters in relaxors. It is shown that the presence of oxygen vacancies impacts more strongly on the incipient ferroic clustering than the degree of long-range B-site ordering. The oxygen deficiency hinders the formation of ferroelectric crystalline-type nanoregions, regardless of the presence/absence of long-range B′/B″-ordered regions. The low degree of defects in the O system enhances the long-range ferroelectric ordering, even in entirely B-site-disordered materials.

1. Introduction

Relaxors are advanced ferroelectric materials which have been attracting considerable attention due to their multi-functionally, on the one hand, and the complexity of local structural phenomena, on the other hand. The understanding of their structure/property relationships is still one of the challenging problems in modern materials physics. Relaxor-related ferroelectrics exhibit high dielectric permittivity and strong electro-optic and electro-elastic coupling. In contrast to the proper ferroelectrics, relaxors exhibit a diffuse phase transition over a temperature range, strong frequency dependence of the dielectric permittivity maximum and an unusually small remanent polarization [1]. The majority of relaxors are lead-based perovskites (see figure 1) of the general formula $Pb(B', B'')O_3$ (B-site complex) or $(Pb, A')BO_3$ (A-site complex). Recently developed relaxor ferroelectric–normal ferroelectric solid solutions

[5] Author to whom any correspondence should be addressed.

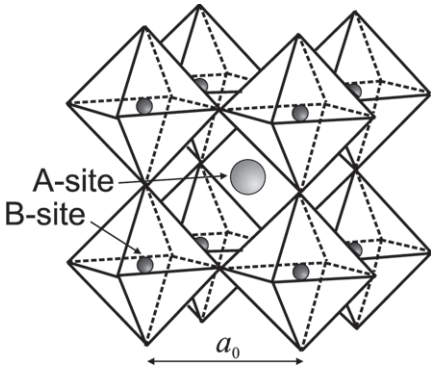

Figure 1. Structural fragment of ideal perovskite structure: corner-sharing BO_6 regular octahedra and a 12-coordinated A-site cation; single perovskites belong to the space group $Pm\bar{3}m$ and have a unit cell parameter $a_0 \approx 4$ Å, whereas double perovskites belong to the space group $Fm\bar{3}m$ and have a unit cell parameter $2a_0 \approx 8$ Å.

with outstanding piezoelectric properties [2] have further increased the interest in this class of materials.

The unique physical properties of relaxors are related to their complex local structure, which strongly deviates from the global, average structure detectable by long-coherent probing radiation like x-ray and high-energy neutron beams. In the vicinity of the dielectric permittivity maximum, relaxors are in a non-ergodic, improper ferroelectric structural state, consisting of polar nanoclusters inside the paraelectric matrix. The clusters interact with each other on an intermediate-range scale only, without leading to the formation of long-range ferroelectric ordering [3]. Because of the small size and short lifetime of the polar nanoclusters [4, 5], studies on relaxor structure require the application of fine-scale, structure-sensitive methods, such as diffuse x-ray scattering, inelastic neutron and light scattering [6–9], in addition to the conventional diffraction methods.

Raman spectroscopy can provide valuable information on ferroic clusters of relaxors by analysing the anomalous signals which, according to the group theory, should not appear in the spectra when we consider the space group of the average structure. However, controversial assignments of the observed Raman peaks have been reported [10–12], and the origin of the corresponding phonon anomalies in the relaxor state is still not clarified. The paraelectric phase of totally B-site-disordered relaxors has a primitive cubic symmetry $Pm\bar{3}m$ with a unit cell parameter ∼4 Å. The 1:1 ordering of the B-positioned cations along ⟨100⟩ directions results in a face-centred cubic $Fm\bar{3}m$ structure with a unit cell parameter ∼8 Å. The phonon modes at the centre of the first Brillouin zone for perovskites with a $Pm\bar{3}m$ symmetry and occupied Wyckoff positions (1a), (1b) and (3d) are $4F_{1u} + F_{2u}$, whereas the corresponding phonon modes for perovskites with $Fm\bar{3}m$ symmetry and occupied Wyckoff positions (4a), (4b), (8c) and (24e) are $A_{1g} + E_g + F_{1g} + 5F_{1u} + 2F_{2g} + F_{2u}$ [13]. Thus no Raman peaks are expected for perovskites with primitive cubic structure, whilst four Raman peaks, generated by A_{1g}, E_g and F_{2g} modes, should be observed for perovskites with face-centred cubic structure. Hence, the Raman activity of relaxors at temperatures above the Curie temperature is mainly associated with the doubling of the perovskite structure due to the presence of compositional B-site order [14]. Very often the nanoscale ferroic clusters are considered in view of their relationship to the long-range B-site ordering. Hence, larger ferroelectric domains are attributed to larger B-site-ordered regions and vice versa. However, the long-range B-site ordering should have negligible influence on the Raman spectra because of the small length scale of the inelastic photon–phonon interaction in

relaxors [15]. Furthermore, doubling of the perovskite structure may occur due to (i) formation of a B-site sublattice, i.e., compositional ordering of B-site cations, and (ii) correlated O-atom shifts along the ⟨100⟩ crystallographic directions (in $Fm\bar{3}m$ the oxygen atoms occupy the (24e) Wyckoff position with fractional coordinates (0, 0, 0.25 + δx) [16]), i.e., ordering of oxygen atoms. The latter may occur on an intermediate-range scale, i.e., in small spatial areas barely detectable by diffraction methods, but well observable by Raman spectroscopy. Recent studies of A-doped and B-doped single crystals of $PbSc_{0.5}Ta_{0.5}O_3$ (PST) showed that there is no apparent correlation between the Raman spectrum features and the degree and size of long-range, B-site-ordered regions [17, 18] and revealed that the presence of additional cations strongly influences the ferroic, nanodomain structure.

Introduction of oxygen vacancies into the perovskite structure also leads to local lattice distortions. One can expect that the presence of oxygen vacancies disturbs the coupling between the ferroic species and thus impacts on the domain structure of relaxors. However, studies on the relationship between the oxygen deficiency and the relaxor behaviour are only sporadic [19]. Herein we report on Raman scattering of $PbSc_{0.5}Ta_{0.5}O_3$ crystals grown under different synthesis conditions in order to obtain crystals with suppressed and enhanced oxygen deficiencies and with different degrees of long-range B-site ordering and, thus to clarify the primary factor for the formation and development of ferroic domains.

2. Experimental details

Single crystals of PST were synthesized by the high-temperature, solution-growth method. Well-shaped, cube-like crystals with a linear size of ∼1 mm were produced in a flux of $PbO:PbF_2:B_2O_3 = 70:29.5:0.5$ in Pt crucibles by two-step cooling: from 1473 to 1223 K in ambient atmosphere and from 1223 to 1193 K in a gas flow. A complete synthesis in a gas flow was impossible due to the instability of the gas ambience at $T > 1223$ K. The synthesis mixture consisted of initially synthesized polycrystalline PST suspended in the flux with a ratio between the solid and liquid phases of 1:10. Four single-crystal samples of PST were analysed throughout this study: they were synthesized in a flow of H_2 or O_2 with a flow rate of 0.2 l h^{-1}, in order to obtain samples with enhanced and suppressed oxygen deficiencies, and using two different cooling rates, 0.3 and 0.5 K h^{-1}, in order to achieve different degrees of B-site ordering in crystals synthesized in the same gas flow. The synthesis conditions for each sample are given in table 1. The crystals grown in H_2 flow were darker and less transparent than those grown in O_2 flow. The ratio of the metal elements of the single crystals obtained was verified by electron microprobe analysis using a Cameca Microbeam SEM system, and no significant deviation from stoichiometry was detected. The room-temperature unit cell parameters and the degree of B-site ordering were determined by powder x-ray diffraction (XRD) analysis using a Philips X'Pert diffractometer. The data are summarized in table 1.

The Raman spectroscopic measurements were performed with a triple monochromator system (Horiba Jobin-Yvon T64000) equipped with an Olympus BH2 microscope. The spectra were collected in back-scattering geometry using the 514.5 nm line of an Ar^+ laser and a beam power on the sample surface of 60 kW cm^{-2}. The Raman scattering was recorded at different temperatures ranging from room temperature to 10 K with a spectral resolution of 2 cm^{-1}. Polarized spectra in four scattering geometries, $Z(XX)\bar{Z}$, $Z(XY)\bar{Z}$, $Z(X'X')\bar{Z}$ and $Z(X'Y')\bar{Z}$ (Porto notation), were measured at each temperature. Herein X, Y, Z, X' and Y' denote directions parallel to the [100], [010], [001], [110] and [$\bar{1}$10] crystallographic directions of a cubic class, respectively. The measured Raman spectra were subsequently reduced by the Bose–Einstein phonon occupation factor to eliminate the temperature dependence in the peak intensities.

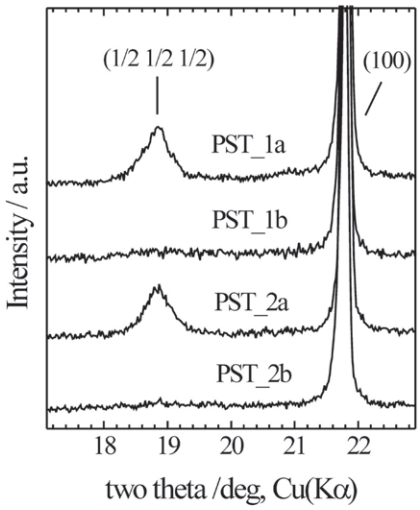

Figure 2. Room-temperature powder XRD patterns of the PST samples studied.

Table 1. Synthesis conditions and structural parameters determined from powder XRD data of the studied PST samples.

	Synthesis conditions				
Sample	Gas	Cooling rate (K h^{-1})	Space group, unit cell parameter a (Å)	Degree of B-site ordering[a]	Domain size[b]
PST_1a	H_2	0.3	$Fm\bar{3}m$, 8.140(5)	0.25	22 nm
PST_1b	H_2	0.5	$Pm\bar{3}m$, 4.076(1)	Entirely disordered	
PST_2a	O_2	0.3	$Fm\bar{3}m$, 8.142(3)	0.24	23 nm
PST_2b	O_2	0.5	$Pm\bar{3}m$, 4.078(2)	Entirely disordered	

[a] Determined as ρ_{exp}/ρ_{theor}, $\rho = I(1/2\ 1/2\ 1/2)I(100)$, according to [20].
[b] From the Scherrer equation applied to the (1/2 1/2 1/2) Bragg reflection.

3. Results and discussion

The powder XRD patterns of the PST samples are shown in figure 2. The samples synthesized with a higher cooling rate (PST_1b and PST_2b) are totally B-site disordered, whereas those synthesized with a lower cooling rate (PST_1a and PST_2a) are partially B-site ordered. The degree of B-site ordering was determined using intensity ratios between the superstructure Bragg reflections related to the $Fm\bar{3}m$ unit cell and the fundamental Bragg reflections of the $Pm\bar{3}m$ primitive cell [20]. Further, the average size of long-range, B-site-ordered domains was calculated from the full width at half maximum of the $Fm\bar{3}m$-related Bragg reflections, using the Scherrer equation for domain-size determination. As can be seen in table 1, the degree of B-site ordering and the average size of B-site-ordered regions is nearly the same for both PST_1a and PST_2a. The XRD data also indicate that the cooling rate may control the compositional B-site ordering in as-synthesized PST crystals. The chemical composition of PST (Sc:Ta ratio = 1:1) is favourable for the formation of B-site-ordered spatial regions. Most probably, the almost twice slower rate of cooling (0.3 versus 0.5 K h^{-1}) facilitates the alternating ordering of Sc and Ta on the surface of the growing crystals.

The $Z(XX)\bar{Z}$ and $Z(XY)\bar{Z}$ spectra of the PST samples measured at room temperature and 10 K are shown in figures 3 and 4, respectively. The simultaneous analysis of these two

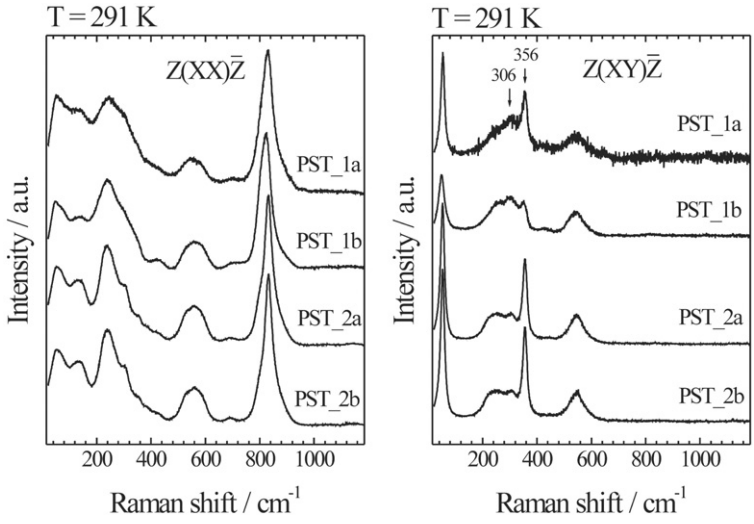

Figure 3. Room-temperature $Z(XX)\bar{Z}$ and $Z(XY)\bar{Z}$ polarized Raman spectra of the studied PST samples. The spectra are normalized to the integrated area of the peak near 830 cm^{-1} measured in $Z(XX)\bar{Z}$ scattering geometry.

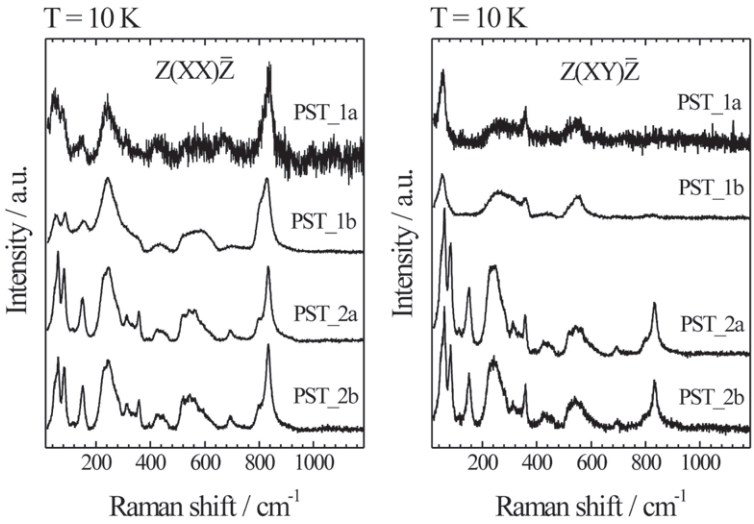

Figure 4. $Z(XX)\bar{Z}$ and $Z(XY)\bar{Z}$ polarized Raman spectra of the PST samples studied, measured at 10 K. The parallel-polarized spectrum of PST_1a is baseline corrected for the strong continuous luminescence-induced background, which occurs below 200 K, using a five-power polynomial function. The spectra are normalized to $I_{pp} + I_{cp}$, where I_{pp} and I_{cp} denote the integrated area of the peak near 830 cm^{-1} measured in $Z(XX)\bar{Z}$ and $Z(XY)\bar{Z}$ scattering geometry, respectively.

scattering geometries yields better understanding of the local structural distortions and allows us to follow the development of the ferroelectric state [21–23]. If the formation of the B′/B″ superlattice is of primary importance for the preferred ferroic clustering and the development of the ferroelectric state, then one would observe a similarity in the Raman scattering between PST_1a and PST_2a, and between PST_1b and PST_2b. However, the Raman scattering data indicate correspondence in the fine-scale structure between the samples synthesized in H_2

flow, PST_1a and PST_1b, and between samples synthesized in O_2 flow, PST_2a and PST_2b, regardless of their difference in the long-range, B-site ordering. Two spectral features have to be addressed: (i) the intensity ratio between the peaks near 356 and 306 cm^{-1} in the room-temperature $Z(XY)\bar{Z}$ spectra, $\rho = \frac{I(356)}{I(306)}$, and (ii) the depolarization of the $Z(XX)\bar{Z}$ and $Z(XY)\bar{Z}$ spectra at low temperatures. Recent high-pressure x-ray diffuse and Raman scattering studies on Pb-based relaxors revealed that the Raman scattering near 350 cm^{-1} is associated with mechanical ordering of the Pb deviations from the cubic positions rather than with compositional B-site ordering [11, 24]. Based on comparative analysis and model calculations of vibrational modes in $PbSc_{0.5}Ta_{0.5}O_3$ and $PbSc_{0.5}Nb_{0.5}O_3$, the Raman scattering in the range 300–360 cm^{-1} has been attributed to Pb–O bond stretching modes activated due to the non-coplanarity of Pb and O atoms in {111} planes [21]. Hence, the intensity ratio ρ is sensitive to the correlation length of coherent Pb shifts along ⟨111⟩ directions. A larger value of ρ indicates a larger size of the quasi-two-dimensional spatial regions in which the Pb atoms are shifted in the same direction with respect to the plane of oxygen atoms; that is, a larger size of the corresponding ferroic species. The intensity ratio ρ for each of PST_1a, PST_1b, PST_2a, and PST_2b, obtained after fitting the spectra with Lorentzians, is 0.49, 0.31, 1.60 and 1.50, respectively. Comparing the samples synthesized in the same gas flow, one can see that the ρ-values of the samples exhibiting long-range B-site ordering, PST_1a and PST_2a, are slightly larger than those of the corresponding samples PST_1b and PST_2b, which show no B-site ordering. However, the apparent difference is that the ρ-values of the samples synthesized in H_2 flow (PST_1a and PST_1b) are significantly smaller than those of the samples synthesized in O_2 flow (PST_2a and PST_2b). Therefore, the presence of oxygen vacancies impacts on the size of incipient ferroic species more strongly than the compositional B-site ordering and the enhancement of oxygen deficiency leads to smaller ferroic nanoclusters.

The primary role of the lack of O deficiency for the development of the long-range ferroic state is also evident from the changes in the parallel and cross-polarized spectra with the temperature decrease (see figure 4). The ferroelectric phase of PST is rhombohedral [25, 26] and, hence, the distortion of the unit cell is along the cubic body diagonal of the prototype structure. Therefore, when crystalline ferroelectric domains occur, the polarized $Z(XX)\bar{Z}$ and $Z(XY)\bar{Z}$ spectra will become nearly the same, since the ferroelectric crystallites, oriented along the eight possible directions ⟨111⟩, will contribute similarly to both scattering geometries. Conversely, if the non-ergodic, improper ferroelectric state, consisting of the isotropic matrix with embedded polar nanoclusters, is preserved, the differences between the parallel and cross-polarized spectra measured with respect to the cubic symmetry should be preserved and only an enhancement of the phonon anomalies should be observed on cooling. Our data reveal a strong resemblance of the Raman scattering measured in $Z(XX)\bar{Z}$ and $Z(XY)\bar{Z}$ experimental geometries at 10 K for the samples synthesized in O_2 flow. At the same time, for the samples grown in H_2 flow, the polarization of the spectra is preserved and only an increase in intensity of some Raman signals (e.g. near 86, 245, 595 cm^{-1}) occurs at 10 K. Therefore, oxygen deficiency restrains the formation of long-range ferroelectric domains, thus favouring the non-ergodic relaxor state, in spite of the presence/absence of compositional B-site ordering.

These observations show that in partially B-site-ordered, Pb-based, perovskite-type relaxors, the degree of oxygen vacancies is more essential for the relaxor structural state than the degree of B-site ordering. Our results are consistent with those reported in [19], demonstrating that oxygen deficiency induces a spontaneous normal-to-relaxor ferroelectric transition in $PbZn_{1/3}Nb_{2/3}O_3$–(Pb, La)(Zr, Ti)O_3 ceramics. Studies on Nb-doped and Ba-containing PST show that the introduction of a second type of B^{5+} or A-site cation leads to similar effects as the oxygen deficiency—a smaller size of the ferroic clusters as

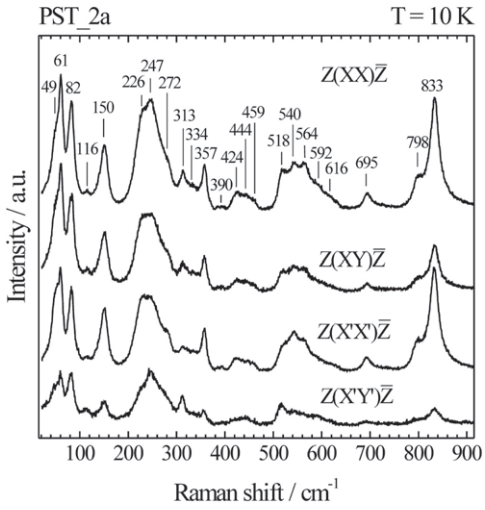

Figure 5. Raman spectra of PST_2a measured at 10 K in four different scattering geometries; X, Y, Z, X' and Y' are the cubic [100], [010], [001], [110] and [$\bar{1}$10] crystallographic directions, respectively. For the sake of comparison, the $Z(XY)\bar{Z}$ and $Z(X'Y')\bar{Z}$ spectra are multiplied by a factor of 2.

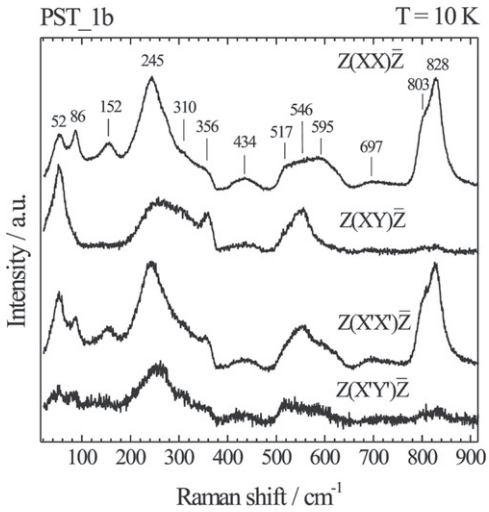

Figure 6. Raman spectra of PST_1b measured at 10 K in four different scattering geometries; X, Y, Z, X' and Y' are the cubic [100], [010], [001], [110] and [$\bar{1}$ 10] crystallographic directions, respectively. For the sake of comparison, the $Z(XY)\bar{Z}$ and $Z(X'Y')\bar{Z}$ spectra are multiplied by a factor of 2.

compared to the ferroic clusters in stoichiometric PST and suppression of the long-range ferroelectric ordering, regardless of the presence of long-range B′/B″-ordered regions [17, 18]. Therefore, the ferroic structural transformations in PST can be controlled independently of the compositional B-site order by inducing point defects in the Pb, B^{5+} or O sublattices.

Figures 5 and 6 show the spectra of the samples with the highest (PST_2a) and lowest (PST_1b) intensity ratios ρ, respectively, measured at 10 K. By analysing the Raman scattering in four different experimental geometries we were able to distinguish unambiguously 23 peaks

for PST_2a. The ferroelectric phase of PST can adopt a double-perovskite-type structure of $R3m$ or $R3$ symmetry [25, 26]. The group theory predicts $7A_1 + 2A_2 + 9E$ optical modes for the $R3m$ symmetry, from which A_1 and E modes are infrared and Raman active, while the A_2 mode is silent [13]. For the $R3$ symmetry all A modes are Raman active. When PST undergoes a paraelectric-to-ferroelectric phase transition near 280 K each cubic triply degenerate mode splits into one single and one doubly degenerate mode. Further splitting of the cubic F_{2g} modes into three components was detected for PST near 180 K, which revealed the occurrence of an additional structural transformation involving further lowering of the rotational symmetry [22]. For sample PST_2a the splitting of the triply degenerate modes of the paraelectric phase into three components appears near 200 K. The splitting is very well pronounced, in particular for the Pb-localized F_{2g}, giving rise to the peaks at 49, 61 and 82 cm^{-1}, the O–B–O bending mode F_{1u} (424, 444, 459 cm^{-1}), and the O–B–O F_{2g} mode (518, 540, 564 cm^{-1}). The detection of such an additional decrease in the structural symmetry also points to a relatively large size of crystalline-type ferroic domains. By comparing the $Z(X'X')\bar{Z}$ and $Z(X'Y')\bar{Z}$ spectra measured at 10 K, one can see that the intensities of most of the peaks are sensitive to the scattering geometries: the band in the range 780–850 cm^{-1}, arising from the BO_6 symmetrical modes, as well as the signals at 564, 540, 424, 357, 226, and 150 cm^{-1}, are stronger in the parallel-polarized spectrum, while the signals at 518, 459, 313, and 116 cm^{-1} are better seen in the cross-polarized spectrum. This is due to the fact that the three-fold symmetry axes of the ferroic nanodomains lie in the same plane or perpendicular to the polarization of the incident light. Thus the spectra collected in $Z(X'X')\bar{Z}$ and $Z(X'Y')\bar{Z}$ geometries mirror to a certain extent the symmetry of the phonon modes of the non-cubic spatial regions: both single and doubly degenerate rhombohedral modes contribute to the parallel-polarized spectrum $Z(X'X')\bar{Z}$, while the cross-polarized spectrum $Z(X'Y')\bar{Z}$ is dominated by atomic vibrations related to doubly degenerate rhombohedral modes. A more precise analysis is, however, hampered by the rather complex nanodomain structure.

The Raman spectra of sample PST_2b (grown in O_2 atmosphere and showing no long-range B-site ordering) follow the same trend on cooling as the spectra of PST_2a do and thus reveal the same structural changes. The latter confirms again that the degree of defects in the oxygen system may affect more strongly the ferroic distortions in relaxors as compared to the chemical ordering.

The spectra of PST_1b contain a smaller number of resolved peaks, and no additional structural transition below the cubic-to-rhombohedral phase transition was deduced from the temperature evolution of the phonon anomalies. The Raman scattering near 830 cm^{-1} is related to the cubic A_{1g} mode, which is allowed to be observed only in parallel-polarized spectra. The appearance of a peak near 830 cm^{-1} in the cross-polarized Raman scattering is indicative of the occurrence of ferroelectric domains. Hence, the absence of pronounced Raman scattering near 830 cm^{-1} in the cross-polarized spectra shows that the paraelectric matrix is the prevalent structural component even at 10 K. The Raman band near 245 cm^{-1} is dominated by the B-cation-localized F_{1u} mode [21, 22]. This mode is Raman inactive in $Fm\bar{3}m$ and contributes to the Raman scattering of PST because of the local structural deviations from the ideal double-perovskite structure. Thus, the increase in its intensity on cooling reveals an enhancement of octahedral off-centre shifts of the B-site cations. The Raman peaks observed in the spectrum of PST_1b have larger widths as compared to the samples grown in an O_2 atmosphere. Apparently, the coupling of atomic displacements is stronger for the samples poor in O vacancies and thus the peaks are sharper, indicating higher structural ordering. It is worth noting the similarities between PST_2a and PST_1b regarding the polarization ratio between in the $Z(X'X')\bar{Z}$ and $Z(X'Y')\bar{Z}$ spectra in the range 500–600 cm^{-1}: for both samples the strongest signal detected in $Z(X'X')\bar{Z}$ and $Z(X'Y')\bar{Z}$ geometry is near 540 and 518 cm^{-1}, respectively. This spectral

range is dominated by BO_6 octahedral bending modes [21]. Therefore, the spectral similarity indicates that nearly the same structural deformation of BO_6 octahedra takes place in both compounds, in spite of the different size of the ferroic regions.

The temperature dependence of the Raman scattering of PST_1a is similar to that of PST_1b. It is worth noting that the effective Raman cross section of PST_1a is smaller than that of the other samples. In addition, when the temperature is decreased a continuum-luminescence background appears, which becomes rather strong below 200 K. Seemingly, the synthesis conditions, reductive ambience and simultaneously slow crystal growth, have facilitated the formation of an abundance of oxygen vacancies in PST_1a, which in turn leads to a high concentration of deep defect electronic levels, giving rise to strong photoluminescence.

4. Conclusions

The data presented reveal that the existence of compositional B-site ordering is not enough for the development of long-range ferroelectric domains. The presence of point defects, such as oxygen vacancies, heavily influences the incipient ferroic clustering and suppresses the formation of ferroelectric crystalline-type nanoregions, thus favouring the relaxor state. On the other hand, the lack of defects in the O system enhances the long-range ferroelectric ordering, even in entirely B-site-disordered materials. Therefore, oxygen deficiency has a stronger effect on the formation of the relaxor state than the degree of long-range, chemical B-site order. Our conclusions should be valid for perovskite-type compounds of the general formula $PbB'_{0.5}B''_{0.5}O_3$, and relaxor behaviour could be induced in other complex perovskites by increasing the number of point defects.

Acknowledgments

Financial support by the Deutsche Forschungsgemeinschaf MI 1127/1-1 and National Scientific Funds—Bulgarian Ministry of Education and Science NT 1-02 is gratefully acknowledged.

References

[1] Bhalla A S, Guo R and Roy R 2000 *Mater. Res. Innovat.* **4** 3
[2] Davis M, Damjanovic D and Setter N 2006 *Phys. Rev.* B **73** 014115
[3] Bokov A A and Ye Z G 2006 *J. Mater. Sci.* **41** 31
[4] Bursill L A, Julin P, Hua Q and Setter N 1995 *Physica* B **205** 305
[5] Blinc R, Gregorovič A, Zalar B and Pirc R 2000 *Phys. Rev.* B **63** 024104
[6] Xu G, Zhong Z, Bing Y, Ye Z-G and Shirane G 2006 *Nat. Mater.* **5** 134
[7] Wakimoto S, Stock C, Birgeneau D J, Ye Z-G, Chen W, Bayer J L, Gehring P M and Shirane G 2002 *Phys. Rev.* B **65** 172105
[8] Husson E 1998 *Key Eng. Mater.* **155/156** 1
[9] Haumont R, Gemeiner P, Dkhil B, Kiat J M and Bulou A 2006 *Phys. Rev.* B **73** 104106
[10] Jiang F, Kojima S, Zhao C and Feng C 2001 *Appl. Phys. Lett.* **79** 3938
[11] Kreisel J, Dkhil C, Bouier P and Kiat J-M 2002 *Phys. Rev.* B **65** 172101
[12] Lina-Silva J J, Guedes I, Mendes Filho J, Ayala A P, Lente M H, Eiras J A and Garcia D 2004 *Solid State Commun.* **131** 111
[13] Bismayer U, Devarajan V and Groves P 1989 *J. Phys.: Condens. Matter* **1** 6977
[14] Siny I G, Katiyar R S and Bhalla A S 2000 *Ferrolectr. Rev.* **2** 51
[15] Rogacheva E A 2000 *Physica* B **291** 359
[16] Dmowski W, Akbas M K, Davies P K and Egami T 1999 *J. Phys. Chem. Solids* **61** 229
[17] Marinova V, Mihailova B, Malcherek T, Paulmann C, Lengyel K, Kovacs L, Veleva M, Gospodinov M, Güttler B, Stosch R and Bismayer U 2006 *J. Phys.: Condens. Matter* **18** L385–93
[18] Güttler B, Mihailova B, Stosch R, Bismayer U and Gospodinov M 2003 *J. Mol. Struct.* **661/662** 469

[19] Deng G, Li G, Ding A and Yin Q 2005 *Appl. Phys. Lett.* **87** 192905
[20] Stenger C G F and Burggaaf A J 1980 *Phys. Status Solidi* a **61** 275
[21] Mihailova B, Bismayer U, Güttler B, Gospodinov M and Konstantinov L 2002 *J. Phys.: Condens. Matter* **14** 1091
[22] Mihailova B, Bismayer U, Güttler B, Gospodinov M, Boris A, Bernhard C and Aroyo M 2005 *Z. Kristallogr.* **220** 740
[23] Mihailova B, Gospodinov M, Güttler B, Stosch R and Bismayer U 2007 *J. Phys.: Condens. Matter* **19** at press
[24] Chaabane B, Kreisel J, Dkhil B, Bouvier P and Mezouar M 2003 *Phys. Rev. Lett.* **90** 257601
[25] Groves P 1985 *J. Phys. C: Solid State Phys.* **18** L1073
[26] Woodward P M and Baba-Kishi K Z 2002 *J. Appl. Crystallogr.* **35** 233